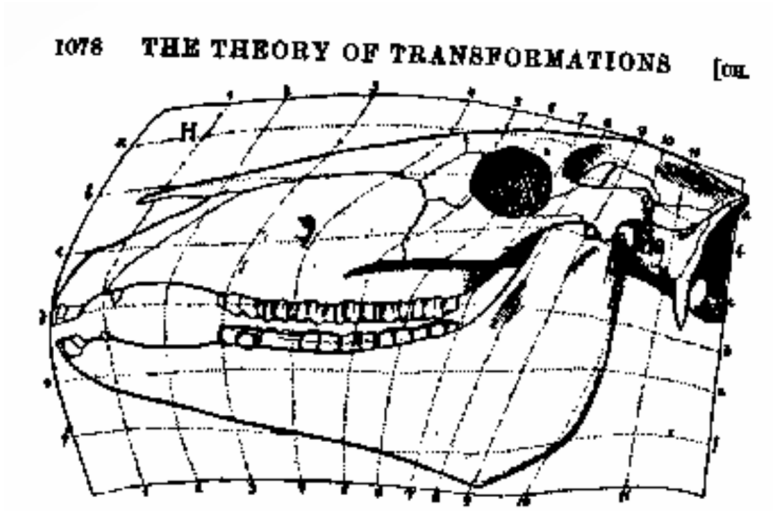

Figure 1. Using a shape transformation for morphometric measurements: (a) Top left: a template of the cross-section of the corpus callosum, a brain structure connecting the two hemispheres. Top middle and right: two individual shapes. Bottom: respective color-coded maps of the determinant of the Jacobian of the shape transformation mapping the template to the two shapes. Contraction is colored green and expansion red. Voxel-wise comparison of these images reveals local shape differences of the respective shapes. (b) Seminal work by D'Arcy Thompson in 1917 using shape transformations to make comparisons among species.

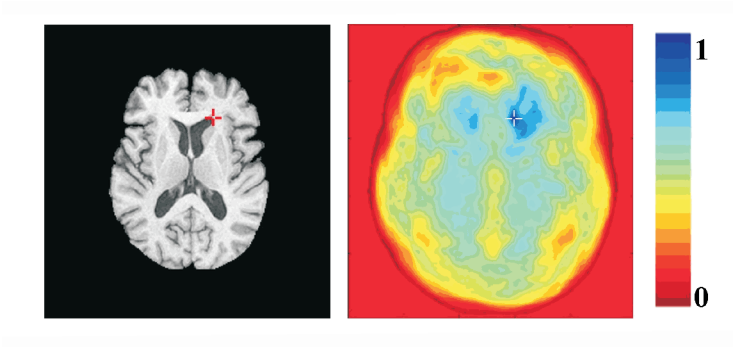

Figure 2. The point marked by a cross has a relatively distinctive GMI-based attribute vector. The color-coded image on the right shows the degree of similarity between the attribute vector of the marked (by crosses) point and the attribute vector of every other point in the brain. 1 is maximum and 0 minimum similarity.

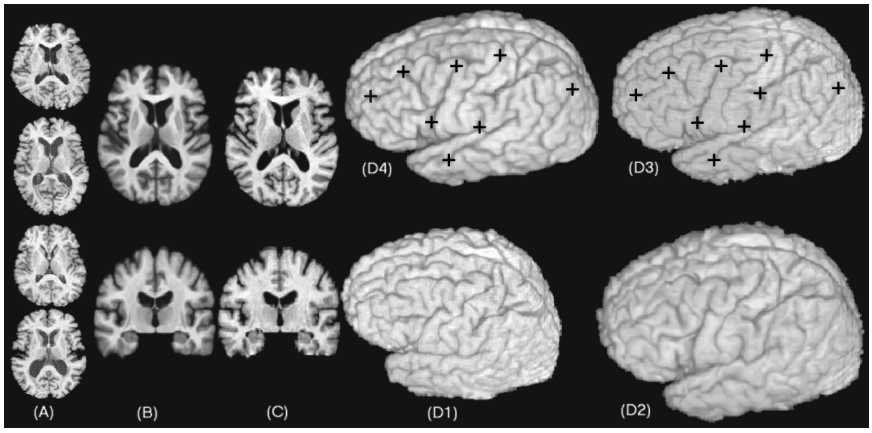

Figure 3. Results using the HAMMER warping algorithm. (a) Four representative sections from MR images of the BLSA database. (b) Representative sections from the image formed by averaging 150 images warped by HAMMER to match the template shown in (c). (d1–d4) 3D renderings of a representative case, its warped configuration using HAMMER, the template, and the average of 150 warped images, respectively. The anatomical detail seen in (b) and (d4) is indicative of the registration accuracy. The red crosses in (d3–d4) are identically placed, in order to allow visualization of point correspondences.

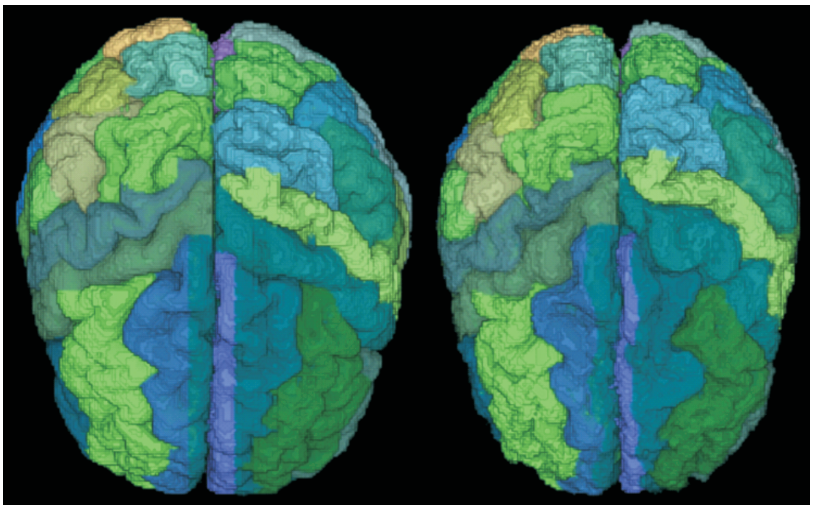

Figure 4. Representative example of automated definition of regions of interest, by warping a pre-labeled atlas (left) to an individual's MR images (the warped atlas is shown on the right as a color-coding of a volume rendering of the target brain). This automated ROI definition makes it possible to apply the method to studies with large sample sizes in a streamlined way.

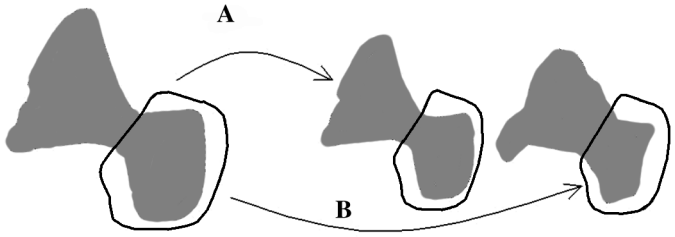

Figure 5. Schematic representation of the mass-preserving framework of the RAVENS analysis. A shape transformation (a) that causes contraction of the structure as it maps it to a stereotaxic space increases the tissue density within the structure, so that the total amount of tissue is preserved. The transformation (b) is different (e.g., it might correspond to a result with greater error in the shape transformation). However, the total amount of tissue is preserved under both transformations, (a) and (b). For example, integrating the tissue density within the outlined regions gives exactly the same result, and is equal to the area of the outlined region in the original shape. This property is lacking in direct measurements of the shape transformation.

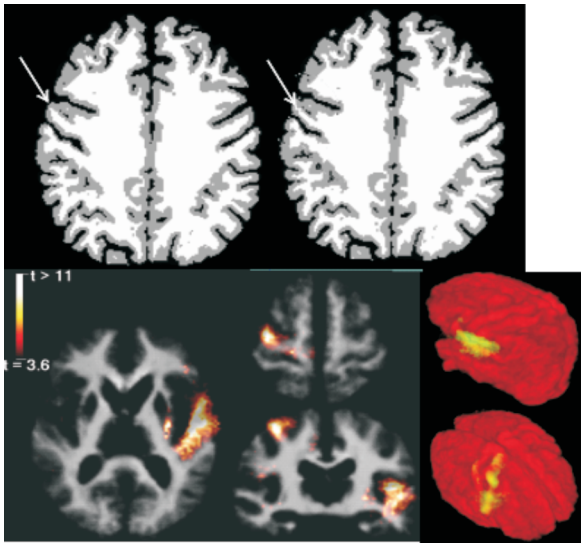

Figure 6. Top: representative slices from the level of the precentral gyrus, with simulated atrophy indicated by the arrows (left = before, right = after uniform 30% atrophy within the gyrus was applied). Bottom: regions detected by the RAVENS analysis, overlaid on the average WM RAVENS maps of the 24 individuals. The two detected regions were exactly where atrophy was simulated. Reprinted with permission from [2]. Copyright ©2001, Academic Press.

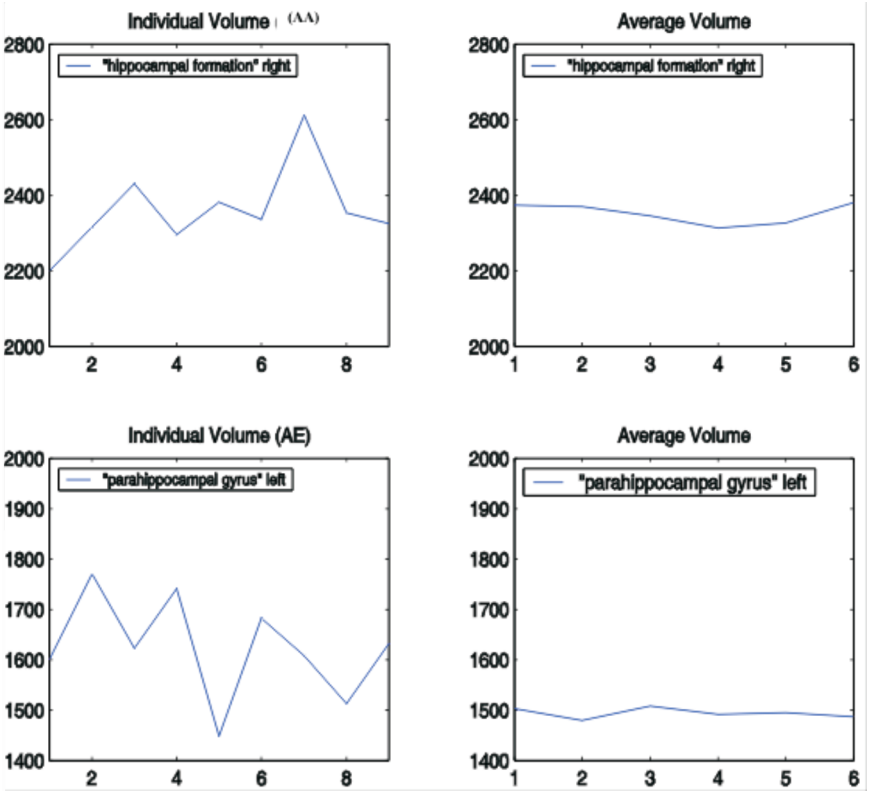

Figure 7. Example illustrating the problems faced when applying a 3D atlas warping method independently to each time-point in a longitudinal study. Left: plots of volumetric measurements from two representative BLSA participants and two structures, using 3D HAMMER (right hippocampal formation and left parahippocampal gyrus). Right: analogous plots showing average volumes of these two structures, obtained by averaging the volumetric measurements of 90 BLSA participants for each of 6 years. Considerable variation is apparent. For example, the standard deviation around the baseline is about 5% for the left hippocampus of subject AD. Although a difference of 5% cannot be appreciated by visual inspection (see Figure 8, below), it can adversely affect the accuracy of longitudinal measurements. As should be expected, variation of the average hippocampal volume is much lower (less than 1%) because of the averaging over 90 individuals.

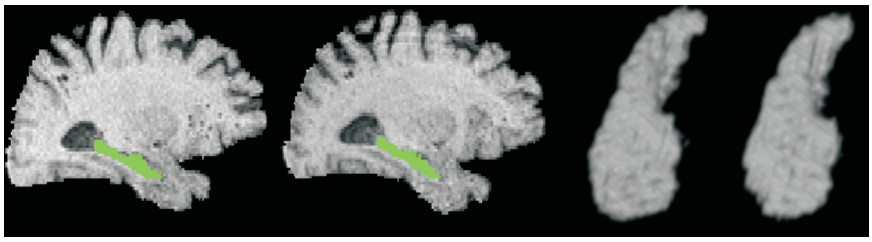

Figure 8. Automated segmentation results using 3D HAMMER for subject AD, years 3 and 4 (see Figure 15, top left). The 5% difference in volumes, in this case, is not readily appreciated visually from these images. (The sections are only approximately corresponding, since the scans were at slightly different orientations. 3D renderings are shown on the right.) Reprinted with permission from [3]. Copyright ©2001, Society for Neuroscience.

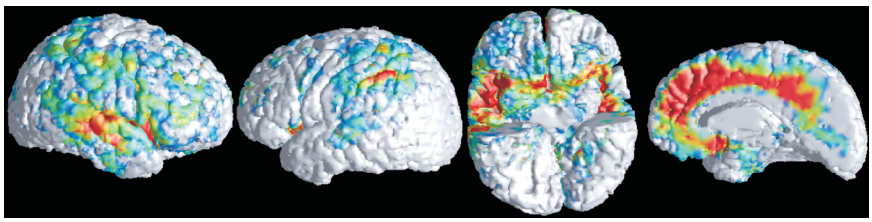

Figure 9. Regions displaying significant longitudinal gray matter atrophy over a 4-year period. Estimates of longitudinal atrophy were determined by segmentation into GM, WM and CSF, then applying the mass-preserving RAVENS methodology described in the text, which deforms each individual's brain into alignment with a template brain, while preserving tissue mass by converting it to density. Voxel-based analysis of the resultant tissue density maps is equivalent to voxel-based volumetric analysis and therefore of atrophy quantification. Reprinted with permission from [3]. Copyright ©2001, Society for Neuroscience.

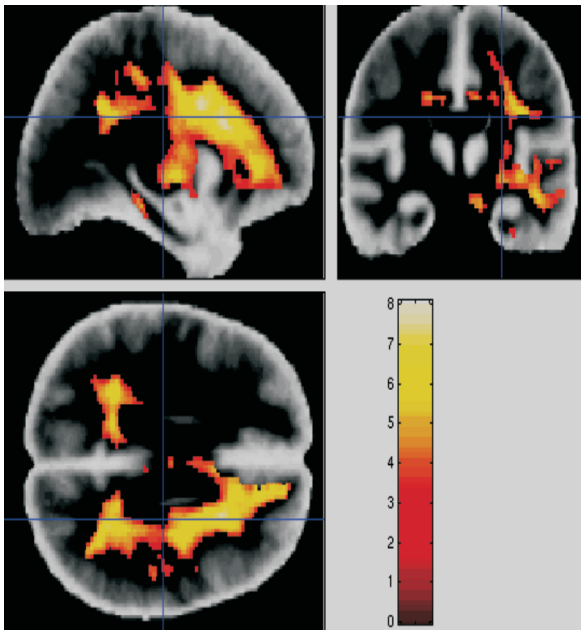

Figure 10. Statistical parametric maps of T1 signal darkening with normal aging, obtained using the RAVENS methodology for elastic registration. T1 darkening might be due to a variety of factors, such as vascular disease, demyelination, mineral deposition, or other degenerative processes. Reprinted with permission from [1]. Oxford UP.

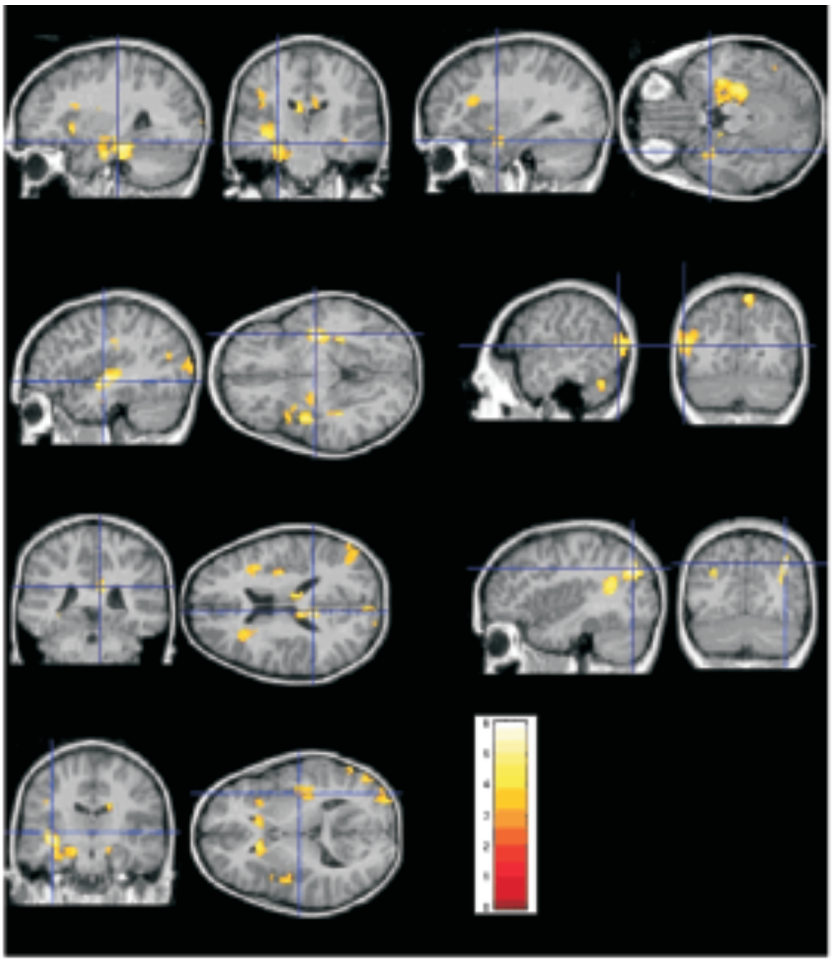

Figure 11. A visual summary of several detected regions with significant group differences between XXY brains and normal control brains. The underlying image is the template that we used to normalize individual brains. Color-coding was based on the values of the t-statistic. Only the voxels with significant group differences, i.e., the corrected p-values exceeding a significance threshold 0.005, are shown. (a) left hippocampal formation; (b) left superior temporal gyrus; (c) cingulate region; (d) left insula; (e) right amygdala; (f) left middle temporal gyri; (g) right parietal lobe WM. Reprinted with permission from [2].

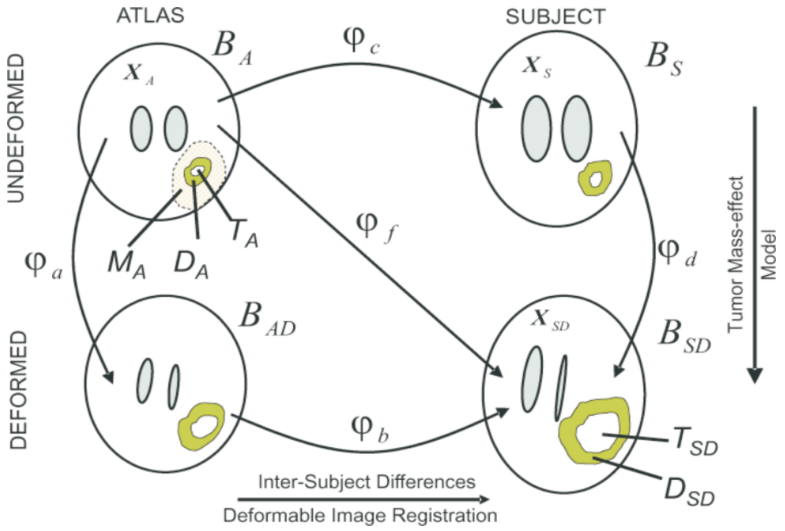

Figure 12. Illustration of the deformation maps involved in the proposed approach. φ_f is the map from the atlas to a subject's tumor-bearing image. Regions T_{SD} and D_{SD} denote the bulk tumor and edema regions in the subject's images, and T_A, D_A are the corresponding regions in the atlas. φ_c is the mapping from the atlas to the subject's image before tumor mass-effect simulation (B_S is not known for non-simulated cases), and φ_d is that obtained through simulation of the tumor mass-effect. Simulating the tumor mass-effect on the atlas results in φ_a and a deformed atlas image that can then be registered to the deformed subject's image through φ_b.

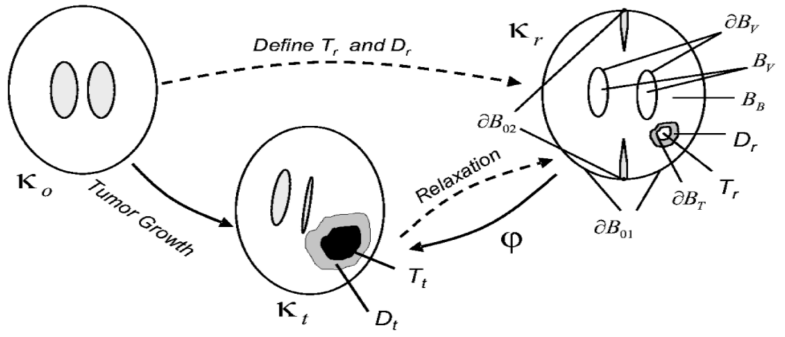

Figure 13. A schematic showing the three configurations involved in the model. κ_o is the brain before tumor development, κ_t is the brain at the desired stage of tumor growth, and κ_r is the corresponding relaxed configuration. T_t and D_t are the bulk tumor and peri-tumor edema regions in κ_t, respectively, while T_r and D_r are the corresponding regions in κ_r. In κ_r, the ventricles are denoted by B_V. ∂B_{01} denotes the outer surface of the brain except for ∂B_{02}, where the falx meets the skull.

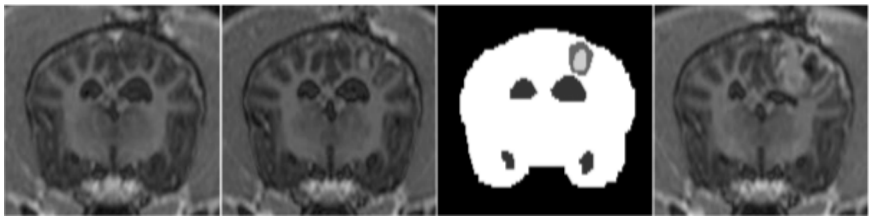

Figure 14. Corresponding 2D images from volumetric gadolinium-enhanced MPRAGE scans of DC1. Left to right: before tumor implantation, 6 days post-implantation, segmentation of the 6 days post-implantation image, and 10 days post implantation

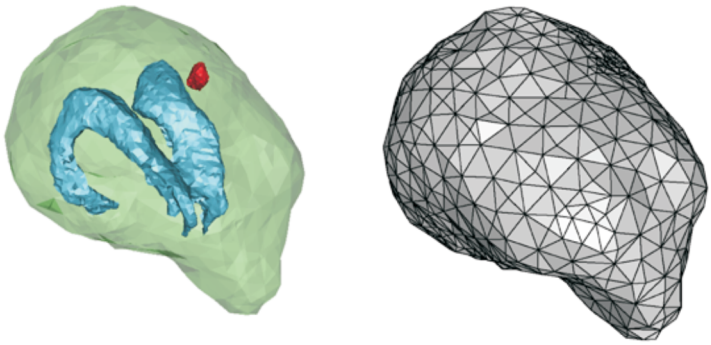

Figure 15. Two views of the FE mesh generated for DC1. Left: outer brain surface mesh; right: translucent outer brain surface and colored surfaces of the tumor and the ventricles.

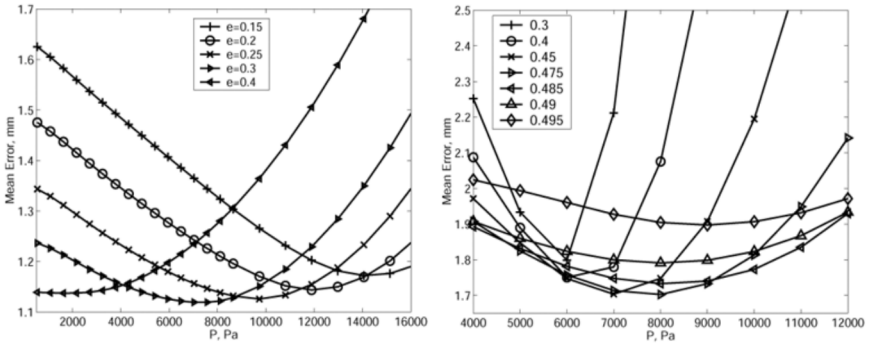

Figure 16. Example curves of the mean errors in the displacement of landmark points for two cases in the dataset. (a) Curves for DC1 at different values of P and e, and for $\upsilon = 0.49$. (b) Curves for HC at different values of P and υ, and $e = 0.3$.

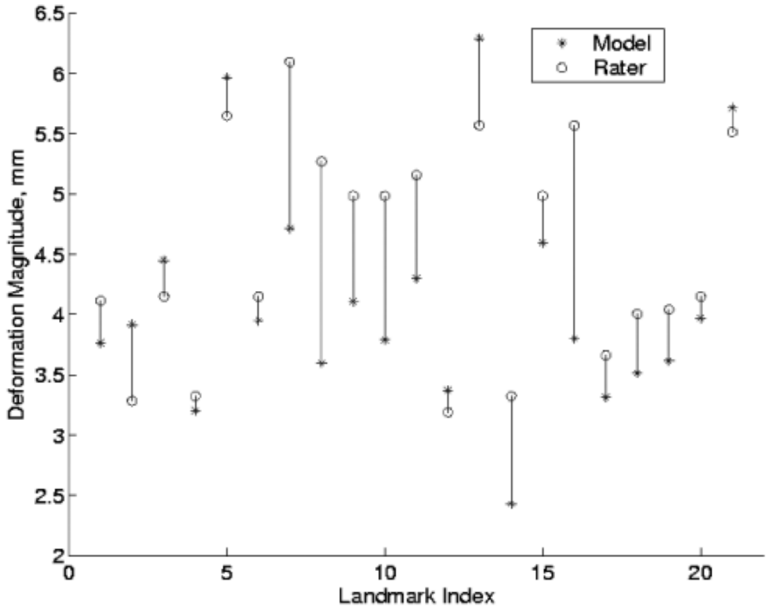

Figure 17. Comparison of the magnitude of deformations of landmarks predicted by the model and the rater for the HC tumor case.

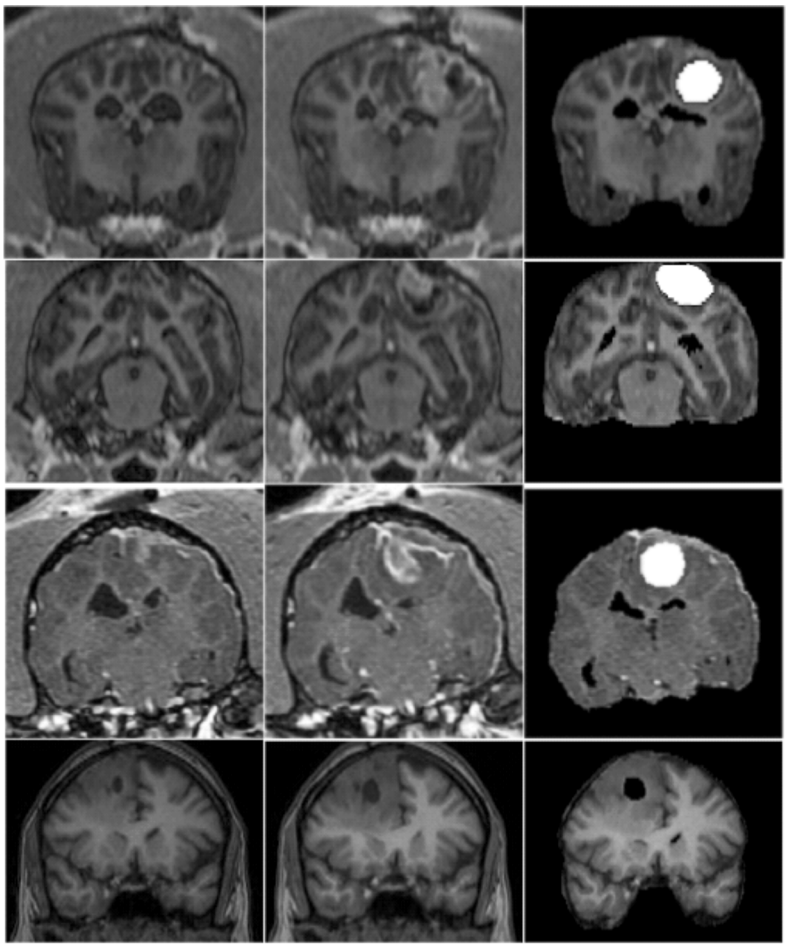

Figure 18. Example cross-sectional images from the starting (left column) and target (middle column) 3D images for all four tumor cases are compared to the deformed images obtained via the optimal parameter values (right column). Rows 1–4 are for DC1, DC2, DC3, and HC, respectively. Tumors in the dog cases are painted white in order to aid visual comparison to the gadolinium-enhanced final images. For HC, the tumor is assigned black.

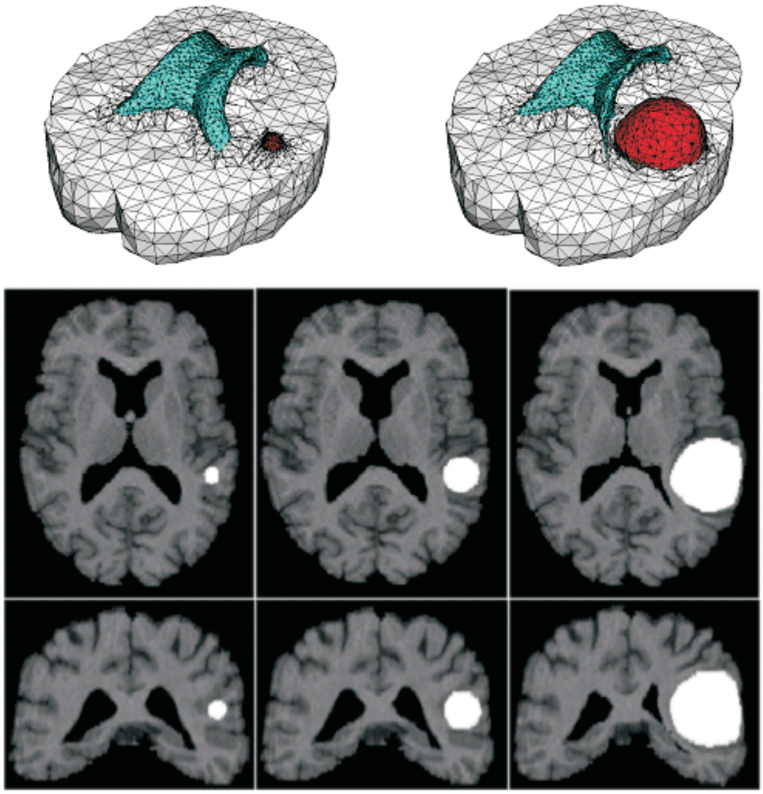

Figure 19. The top row shows a clipped view of an FE mesh generated from volumetric images of a healthy human subject. Surfaces of the ventricles (cyan) and tumor (red) are added. The left image illustrates the mesh at the beginning of the simulation, and the right image illustrates the mesh at termination. The bottom two rows provide transaxial (middle row) and coronal (bottom row) 2D slices of the volumetric images at the beginning of the simulation (left) and at termination (right). One-time remeshing was used halfway through application of pressure P. The middle column shows images from a simulation in which remeshing was not used. This simulation terminated before reaching the final value of P.

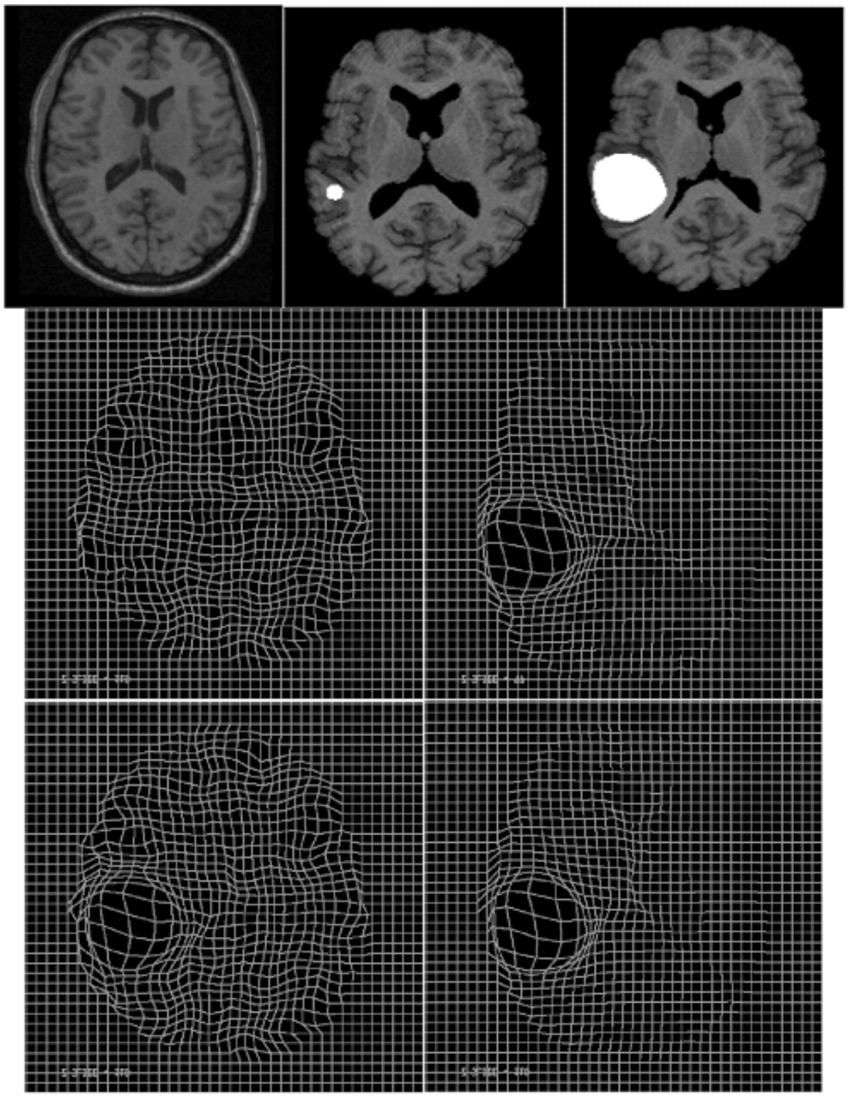

Figure 20. Illustration of a tumor mass-effect simulation and the associate displacement maps. Top row (left to right): atlas image, normal subject's MR image with an introduced small tumor, and resulting image after simulation of tumor mass-effect. Middle row: displacement map $\mathbf{u}_c$ (left) and displacement map $\varphi_d - \mathbf{X}_S$ (right). Bottom row: displacement map $\mathbf{u}_d$ (left) and displacement map $\mathbf{u}_c$ (right).

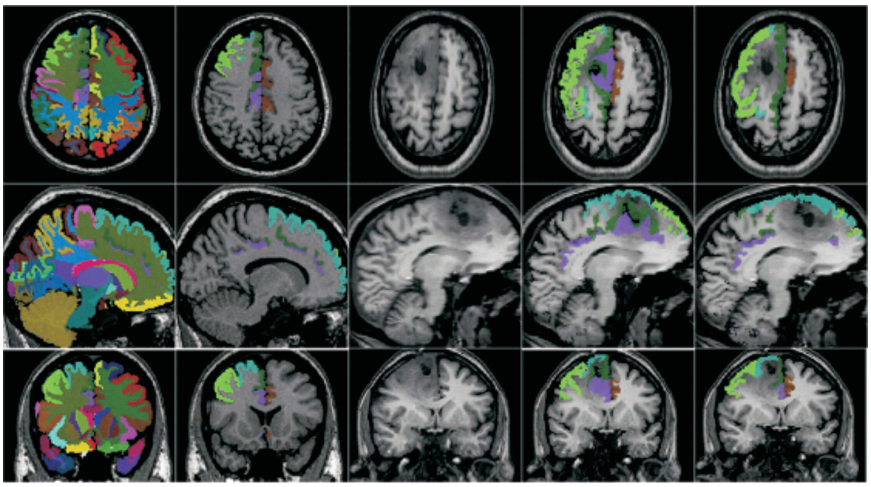

Figure 21. Three orthogonal 2D images of the atlas and the real tumor patient before and after deformable registration. Some labels associated with the atlas image are warped and superimposed on the patient's images. Left to right: atlas image with all labels; atlas image with five selected labels near the tumor area; patient's image; patient's image with superimposed labels warped from the atlas via direct deformable registration between the two images; and the patient's image with superimposed labels warped from the atlas via the proposed approach. The five selected labels are: the right middle frontal gyrus (green), the right medial frontal gyrus (dark green), the right superior frontal gyrus (cyan), the right cingulate region (magenta), and the left cingulate region (brown).

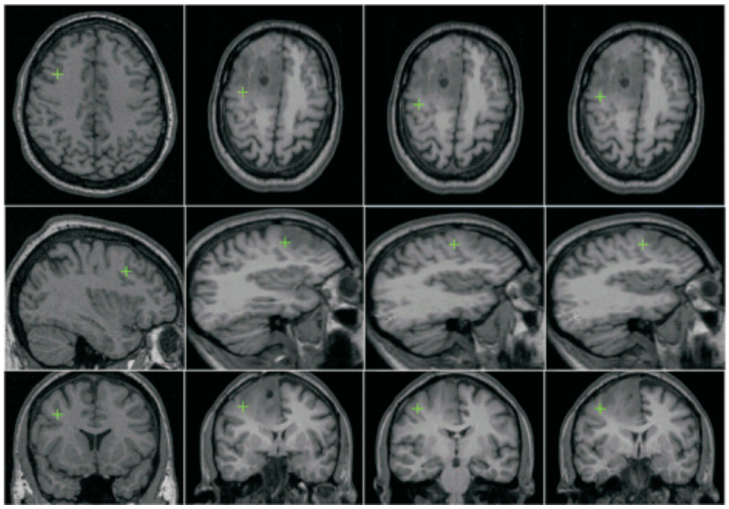

Figure 22. Locations of one manually selected landmark point in three orthogonal 2D images of the atlas and the patient before and after deformable registration. The landmark point is marked with a green cross. Left to right: atlas image, patient's image with the manually selected landmark point; patient's image with the warped landmark point from the atlas with direct use of deformable registration; and the patient's image with the warped landmark point from the atlas with the proposed approach.

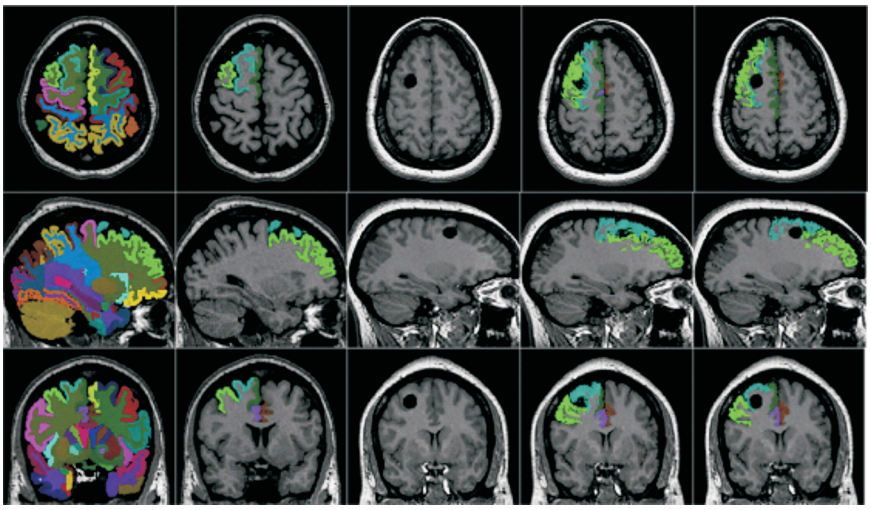

Figure 23. Three orthogonal 2D images of the atlas and the simulated tumor subject before and after deformable registration. Some labels associated with the atlas image are warped and superimposed on the subject's images. Left to right: atlas image with all labels; atlas image with five selected labels; subject's image; subject's image with superimposed labels warped from the atlas via direct deformable registration between the two images; and the subject's image with superimposed labels warped from the atlas via the proposed approach. The five selected labels are the same as those shown in Figure 21 for the real tumor case.